Eur. Phys. J. D **5**, 389–403 (1999)

**THE EUROPEAN PHYSICAL JOURNAL D**

EDP Sciences


# Photoassociative spectroscopy of the $Cs_2\,0_g^-$ long-range state

A. Fioretti, D. Comparat, C. Drag, C. Amiot, O. Dulieu[a], F. Masnou-Seeuws, and P. Pillet

Laboratoire Aimé Cotton[b], Université Paris-Sud, Bâtiment 505, 91405 Orsay Cedex, France

Received: 20 May 1998 / Revised: 1st August 1998 / Accepted: 5 November 1998

**Abstract.** The photoassociative spectroscopy of the $Cs_2$ $0_g^-$ long-range molecular state dissociating into the $6s\ ^2S_{1/2} + 6p\ ^2P_{3/2}$ asymptote is performed, using cold cesium atoms in a vapor-cell magneto-optical trap (MOT). Vibrational levels from $v = 0$ to $v = 132$ are identified, and their rotational structure is well resolved up $J = 8$ for levels below $v = 74$. These data are analyzed in terms of the Rydberg-Klein-Rees (RKR) procedure, and correspond to 99.6% of an effective potential curve with a minimum at $12.36 \pm 0.05$ Å and a $77.94 \pm 0.01$ cm$^{-1}$ depth. Both *ab initio* calculations and simple model estimations predict a double-well structure for this potential curve, which cannot be reproduced presently by the RKR approach but which is confirmed by the presence of giant structures in the spectrum. The $1_u(6s\ ^2S_{1/2} + 6p\ ^2P_{3/2})$ long-range state is also observed for the first time in $Cs_2$.

**PACS.** 32.80.Pj Optical cooling of atoms; trapping – 33.20.-t Molecular spectra – 34.20.-b Interatomic and intermolecular potentials and forces, potential energy surfaces for collisions

## 1 Introduction

Determination of the long-range interactions between two neutral atoms have long been the object of a substantial effort [1]. During the past decade, developments in laser cooling and trapping of atoms has opened the way to photoassociative spectroscopy of alkali dimers [2], yielding accurate determinations for the long range part of molecular potential curves, in particular those correlated with the ground $s + s$ or the first excited $s + p$ asymptotes. The knowledge of these data is crucial in the interpretation of many new physical phenomena associated with cold atom dynamics, as for instance the prediction of the stability of Bose-Einstein condensates [3–5] which depends upon the ground state scattering lengths.

Molecular photoassociation (PA) of cold atoms has been demonstrated for all alkali atoms [6,7], but only very recently for the cesium atom [8]. Due to their very low relative kinetic energy ($k_BT \leq 1$ mK $\simeq 21$ MHz), two free cold atoms can absorb a photon with a resonant wavelength, to create an excited molecule in a well-defined rovibrational state. As the Franck-Condon principle favors the excitation of vibrational levels close to the dissociation limit, the PA of cold atoms supplies a new high resolution method complementary to the traditional bound-bound laser spectroscopy, which is in most cases devoted to lower levels. The combination of both methods can lead to the complete description of a potential curve, and to the determination of dissociation energies [9] or atomic radiative lifetimes [10–12] with an extremely high accuracy.

In a previous letter [8] we have reported on the first observation of molecular PA of cold cesium atoms in a vapor-cell magneto-optical trap. In this first experiment we have observed 63 lines ranging 10 cm$^{-1}$ below the $6s\ ^2S_{1/2} + 6p\ ^2P_{3/2}$ dissociation limit. Four accessible Hund's case (c) long-range attractive potential curves ($1_g$, $0_u^+$, $0_g^-$ and $1_u$) are converging towards this limit, and these lines have been attributed to rovibrational levels of the $0_g^-$ state. The originality of the experiment was in the detection of $Cs_2^+$ molecular ions by photoionization of $Cs_2$ triplet ground state molecules, produced by spontaneous decay of the excited molecular state formed by photoassociation. Such molecules are indeed observed during their fall outside the atomic trap, providing the first evidence for the production of translationally cold molecules. The ballistic expansion of the molecular cloud has allowed us to determine a temperature of roughly 300 $\mu$K for the molecular sample, close to the estimated temperature of the initial atomic cloud ($\sim 200$ $\mu$K). The formation of cold molecules in a photoassociative scheme (Fig. 1) is linked to the particular shape of the $0_g^-$ potential curve, which presents a Condon point at intermediate internuclear distances due to its double-well structure. This allows an efficient stabilization of cold molecules through spontaneous emission towards the lowest $^3\Sigma_u^+$ electronic state.

In this article, we report on the photoassociative spectroscopy of the $0_g^-$ long-range state over a 80 cm$^{-1}$ energy range below the $6s\ ^2S_{1/2} + 6p\ ^2P_{3/2}$ dissociation limit. This involves the measurement of the energies of

[a] e-mail: dulieu@perceval.lac.u-psud.fr
[b] CNRS II

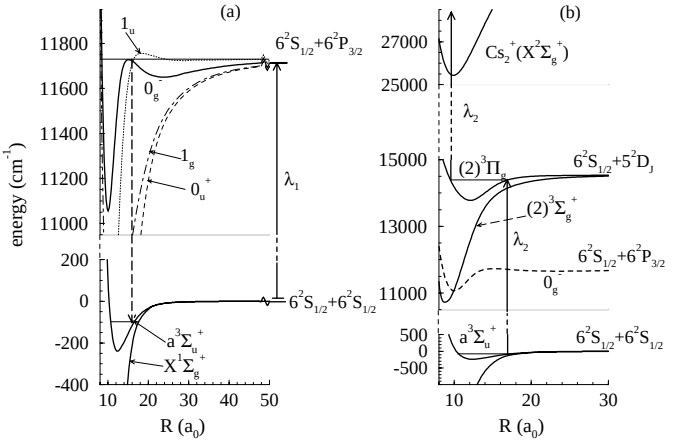


**Fig. 1.** Optical transitions relevant for the present experiment. (a) Photoassociation and spontaneous decay indicated for the $0_g^- \rightarrow a^3\Sigma_u^+$ transition. (b) Resonant two-photon ionization of the $a^3\Sigma_u^+$ levels. All potential curves are built from *ab initio* [55,56] and asymptotic [29,30] calculations.

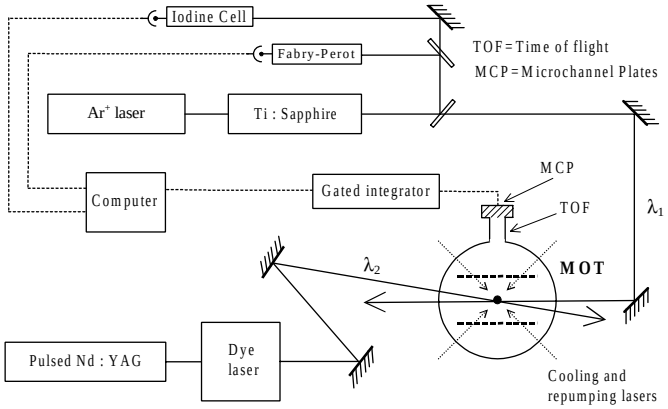


**Fig. 2.** Scheme of the experimental setup. The optical and laser setup for the MOT is not shown, as well as the two vertical trapping laser beams.

the first 133 vibrational levels, with rotational structure resolved up to $v = 74$. These energies are fitted in the framework of the Rydberg-Klein-Rees (RKR) approach, providing 99.6% of the energy depth of an effective potential curve with a minimum at $12.36 \pm 0.05$ Å, and a $77.94 \pm 0.01$ cm$^{-1}$ total depth. The RKR potential curve is discussed and compared to asymptotic model estimations and quantum chemistry computations, which predict a double-well shape for this state. The $0_g^-$ long-range state in $Cs_2$ cannot be considered as a "pure long range state", as defined by Stwalley *et al.* [13], as the hump between the two wells is influenced by short-range molecular forces.

The paper is organized in the following way: the experimental approach is described in Section 2 and the measurements of the energies of the detected $0_g^-$ ro-vibrational levels are reported in Section 3. The basic principles of the fitting procedure are recalled in Section 4, yielding the best possible potential curve for representing the data. The RKR potential curve is compared in Section 5 with the potential curve computed by matching the asymptotic long-range $0_g^-$ curve with the *ab initio* short range $0_g^-$ curve. The origin of the double-well structure of the upper $0_g^-$ curve of the cesium dimer is also carefully discussed using asymptotic expansion.

## 2 Experimental setup

The principle of the experiment has been described in reference [8], and is recalled here for clarity. The cold Cs atoms of a vapor cell magneto-optical trap (MOT) are illuminated with a cw laser to produce photoassociation. The experimental setup, already partly described in reference [14], is schematized in Figure 2. The cold atoms are produced in a vapor loaded MOT [15], at the intersection of three pairs of mutually orthogonal, counter-propagating $\sigma^+ - \sigma^-$ laser beams of intensity nearly 2 mW/cm$^2$ (to be compared with the saturation intensity $I_s = 1.1$ mW/cm$^2$), at the zero magnetic field point of a pair of anti-Helmholtz coils with a magnetic field gradient of 15 Gauss/cm. The residual pressure is $2 \times 10^{-9}$ torr. The cooling and trapping laser beams are split from a slave diode laser (SDL 5422-H1, 150 mW, single mode, $\lambda \sim 852$ nm) injection locked to a master diode laser. The master laser (SDL 5412-H1, 100 mW) is frequency-narrowed by optical feedback from an extended, grating ended, cavity. Locking the master laser frequency to a saturated absorption line of a cesium vapor ensures its long-term stabilization. The trapping laser frequency is tuned about 13 MHz ($\simeq 2.5$ natural linewidths) on the red of the frequency $\nu_{4\rightarrow5}$ of the $6s\ ^2S_{1/2}(F = 4) \rightarrow 6p\ ^2P_{3/2}(F' = 5)$ atomic transition. A repumping laser beam (SDL 5712-H1, 100 mW, $\lambda \sim 852$ nm) of frequency $\nu_{3\rightarrow4}$ resonant with the $6s\ ^2S_{1/2}(F = 3) \rightarrow 6p\ ^2P_{3/2}(F' = 4)$ transition is superimposed with two of the beams of the cooling laser, preventing atoms to be optically pumped in the untrapped $F = 3$ hyperfine ground state. In these conditions, the dimension (FWHM) of the cold sample ranges between 400–600 $\mu$m, the number of atoms in the trap ranges between $1-5 \times 10^7$, thus leading to a peak density of the order of $10^{11}$ atoms/cm$^3$. The estimated temperature of the cold atomic sample is $T \simeq 200$ $\mu$K [16].

In the first experiment [8], the cold Cs atoms were continuously illuminated by the beam of a diode laser ($\lambda \sim 852$ nm, SDL 5712-H1, 100 mW) focused on a diameter of 100 $\mu$m, yielding a disposable intensity for PA in the MOT zone of 200 W/cm$^2$. We were able to scan the wavelength of the laser diode on a 10 cm$^{-1}$ range without mode jumps on the red-side of the trapping transition, by slowly changing the diode temperature.

In the present study, the diode laser has been replaced by a Ti:sapphire laser (Coherent 899 ring laser) pumped by an Argon ion laser, allowing larger detunings of the PA laser frequency. The maximum available power in the experiment zone is 600 mW, focused on a spot with $\sim 500$ $\mu$m diameter. However, the power of the PA laser has been gradually reduced for detunings smaller than about 2 cm$^{-1}$ from $\nu_{4\rightarrow5}$ in order to avoid perturbations

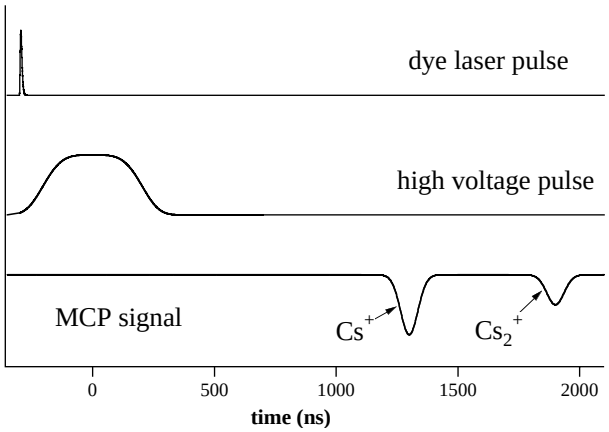


**Fig. 3.** Typical detection time sequence. The time origin is chosen at the center of the high voltage accelerating pulse. The $Cs_2^+$ and $Cs^+$ ion pulses arrival times are in a ratio of $\sim \sqrt{2}$. This sequence has a repetition rate of 10 Hz.

of the MOT operation. The frequency scale is calibrated using a Fabry-Perot interferometer (750 MHz free spectral range), and the absorption lines of iodine [17] (see Fig. 2). The PA laser spectral linewidth is 1 MHz and its frequency can be continuously scanned on a 30 GHz range. The PA laser excitation corresponds to the photoassociative reaction (Fig. 1a):

$$\mathrm{Cs}\ (6s\ ^2S_{1/2}, F=4) + \mathrm{Cs}\ (6s\ ^2S_{1/2}, F=4) + h\nu_1 \rightarrow \mathrm{Cs}_2\ (0_g^-(6s\ ^2S_{1/2} + 6p\ ^2P_{3/2}; v, J)). \quad (2.1)$$

As we have already mentioned, the photoassociative excitation of the $Cs_2$ $(0_g^-(6s\ ^2S_{1/2}+6p\ ^2P_{3/2}; v, J))$ state produces, by spontaneous emission, transitionally cold $Cs_2$ molecules in their lowest triplet state $a^3\Sigma_u^+$. Evidence of the photoassociative process is detected by ionization of the cold molecules into $Cs_2^+$, using a pulsed dye laser (dye: LDS 722; pulse duration 7 ns; pulse energy: 1 mJ) pumped by the second harmonic of a Nd-YAG laser, running at 10 Hz repetition rate. The dye laser is tuned at the wavelength $\lambda_2 \sim 716$ nm. The ionization process (Fig. 1b) is a resonant two-step photoionization *via* the vibrational levels of an electronic molecular state correlated to the $6s\ ^2S_{1/2} + 5d\ ^2D_{3/2,5/2}$ dissociation limit. The detection temporal sequence is shown in Figure 3. At the trap position, a pulsed high-voltage field (4.15 kV, 0.5 $\mu$s) is applied by means of a pair of electric field grids spaced 15 mm apart. The produced $Cs^+$ and $Cs_2^+$ ions are expelled out of the interaction region in a 6 cm field-free zone constituting a time-of-flight mass spectrometer separating in time $Cs_2^+$ ions (1.9 $\mu$s delay) from $Cs^+$ ones (1.3 $\mu$s delay) (Fig. 3). The ions are detected by a pair of micro-channel plates and the $Cs_2^+$ ion signal is recorded with a gated integrator. The whole acquisition is controlled by a computer running with the Labtech software.

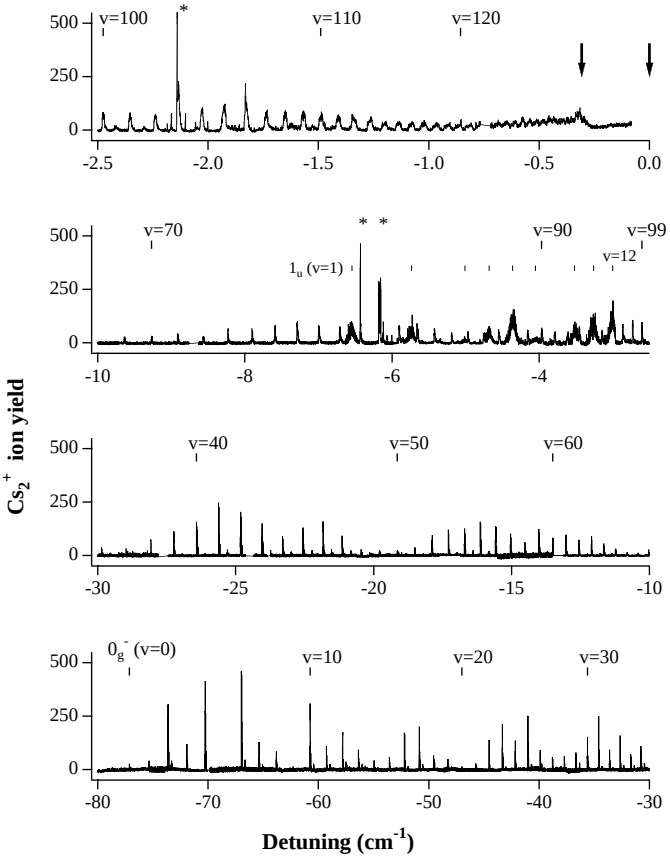


**Fig. 4.** Experimental spectrum of $Cs_2^+$ ions as a function of the PA laser frequency. Near the origin the PA laser destroys the MOT. The two arrows, respectively at $\delta^{exp} = 0$ and $\delta^{exp} = -0.375$ cm$^{-1}$, indicate the two molecular hyperfine dissociation limits $6s\ ^2S_{1/2}(F=3) + 6p\ ^2P_{3/2}(F'=4)$ and $6s\ ^2S_{1/2}(F=4) + 6p\ ^2P_{3/2}(F'=5)$. The spectrum is the result of over 200 single 30 GHz scans with slightly different experimental conditions and noise level. Points separation is 15 MHz. Data are renormalized to absolute ion counts. Levels of the $0_g^-$ series are indicated by thick bars and those of the $1_u$ series with thin ones. Stars indicate the three "giant" lines. Counts on the first "giant line" are out of scale.

## 3 Experimental spectrum

The $Cs_2^+$ ion spectrum is recorded as a function of the PA laser frequency, over a 80 cm$^{-1}$ range (Fig. 4). The origin of the energy scale is fixed at the $6s\ ^2S_{1/2}(F=4) \rightarrow 6p\ ^2P_{3/2}(F'=5)$ atomic transition, which corresponds to an energy of 11 732.183 cm$^{-1}$ [18] above the $6s\ ^2S_{1/2}(F=4) + 6s\ ^2S_{1/2}(F=4)$ asymptote. For detunings smaller than 0.1 cm$^{-1}$, the MOT is destroyed by the PA laser. The position of 133 lines has been determined with a maximum absolute uncertainty of $\pm$ 300 MHz, mainly due to the uncertainties on the position of the iodine lines. They cover a range of detunings from 0.4 cm$^{-1}$ to $-77.12$ cm$^{-1}$. The absolute maximum uncertainty within the first 5 cm$^{-1}$ is estimated to be better than $\pm$ 150 MHz due to the calibration with the atomic Cs lines. Moreover the frequency difference of two vibrational lines belonging to a

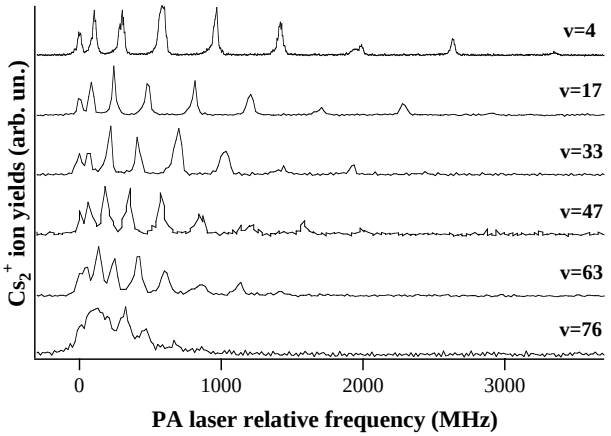


**Fig. 5.** Details of the rotational structure of different $0_g^-$ levels. The hyperfine structure becomes larger for higher values of $v$ while the rotational structure decreases.

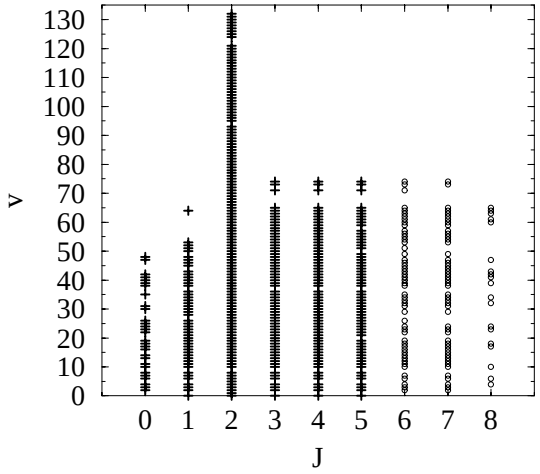


**Fig. 6.** The $(v, J)$ data set of the observed PA spectrum. Levels used in the fit "$F_2$" are shown with crosses.

same scan of the Ti:sapphire laser is determined with an uncertainty smaller than ± 50 MHz. For detunings larger than 8 $cm^{-1}$ the rotational structure of the lines is resolved with a ± 7 MHz accuracy in the relative position of each rotational component.

According to the RKR analysis of Section 4, the line with the largest detuning ($-77.119$ $cm^{-1}$) in Figure 4 has been labeled ($v = 0, J = 2$). Moreover, we have looked for ion signal at larger detunings up to 100 $cm^{-1}$, finding no evidence for further lines. Most of the lines are accompanied by a smaller one at 9.2 GHz to the blue (see for instance the lines near $v = 45$ in Fig. 4), corresponding to a PA process between one Cs ($6s\ ^2S_{1/2}, F = 4$) and one Cs ($6s\ ^2S_{1/2}, F = 3$) atom. This indicates that nearly 5% of colliding cold atoms undergoing photoassociation are in the ($F = 3$) ground hyperfine level. This unusually large fraction of ($F = 3$) atoms is not explained in a normal MOT operation (with a strong and resonant repumping laser) and is due to cooperative effects between the trap laser and the PA laser [19].

For $v > 80$, the width of the resonances is nearly 600 MHz and it can be attributed essentially to the hyperfine structure of the $0_g^-$ state. The rotational structure, enlarged for a few lines in Figure 5, is resolved up to $J = 8$ for most of the vibrational levels below $v = 74$ (Fig. 6). Levels above $v = 74$ have been arbitrarily labeled by $J = 2$ in Figure 6, which is the most intense line in each resolved rotational structure.

In the remaining part of the paper, we will concentrate on the analysis of the energy position of these lines, in order to provide an accurate description of the corresponding molecular state. However, we mention below several other features which are also visible in Figure 4.

1. The modulation in the intensities of the lines, already mentioned in [8], is even better manifested over the larger range of detunings investigated here. As discussed for example in references [2,20–22], it is due to the variation of the Franck-Condon factors for the PA transitions between the initial state of two cold free atoms and the final ro-vibrational levels of the $0_g^-$ state. According to preliminary calculations, the spontaneous decay step and the ionization step do not affect the modulation of the $Cs_2^+$ signal. These data should be considered for the determination of the Cs scattering lengths, which is still an open problem [23, 24]. Our previous analysis [8] gave an absolute value larger than $260a_0$, without determining its sign.
2. In contrast with similar photoassociation experiments [25,26], $J$ values larger than the highest partial wave allowed by the trap temperature (at 200 $\mu$K, only $s$, $p$ and $d$ waves can penetrate into the molecular region) are observed. This is also due to cooperative effects of trap lasers and PA laser, which provide an enhanced flux at short distances of colliding pairs with higher relative orbital angular momenta [19]. This important point is addressed elsewhere [27].
3. Compared to the spectrum observed in our previous study [8], new structures have now emerged in the range of 3–7 $cm^{-1}$ due to the larger intensity available for PA with the Ti:sapphire laser. We assign these structures to levels of the long-range $1_u$ ($6s\ ^2S_{1/2} + 6p\ ^2P_{3/2}$) state (drawn in Fig. 1), observed up to now only in a $K_2$ PA experiment [28]. Asymptotic calculations using parameters from references [29,30] predict for this state $a \simeq 7$ $cm^{-1}$ well depth, $a \simeq 6$ GHz width for the hyperfine structure, and a level spacing which are compatible with the present observations. As for the $0_g^-$ long-range state, the potential curve of the $1_u$ state is also exhibiting a Condon point at intermediate distance (around $25a_0$), such that translationally cold $Cs_2$ molecules are likely produced in their singlet ground state by spontaneous emission.
4. Three "giant" structures are clearly visible in Figure 4. The first one, already observed in our previous work [8], is located on the top of the $0_g^-(v = 103)$ level, at a detuning of 2.140 $cm^{-1}$ (for the $J = 3$ component), and has a large rotational constant of about 140 MHz. The second structure occurs in place of the $0_g^-(v = 79)$ level, at a detuning of 6.153 $cm^{-1}$ (for the $J = 3$ component), with a rotational constant of

$\simeq$ 190 MHz). A preliminary estimation using *ab initio* potentials defined in Section 5.2 suggest that it could be attributed to vibrational levels of the inner well of the $0_g^-$ potential, populated by tunneling through the barrier, and also possibly perturbed by the upper $^3\Sigma_g^+(0_g^-)$ state correlated to $6s\ ^2S_{1/2} + 5d\ ^2D_{3/2}$ (see Fig. 1b). The third structure at a detuning of 6.430 $cm^{-1}$ has no resolved rotational structure. We shall exclude these data from the $\{E(v, J)\}$ set of measured energies analyzed in the next section, attributed to levels lying in the $0_g^-$ external well.

## 4 Data representation and fitted potential energy curve

The quality of data representation can be judged by the four criteria put in evidence by Tromp and Le Roy [31]: accuracy, physics, compactness and extrapolation ability. The problem is to construct an accurate potential curve giving a compact physical representation of the observed rovibrational $E(v, J)$ energy values. A usual approach is the Rydberg-Klein-Rees (RKR) method, which determines the inner ($R_-$) and outer ($R_+$) turning points of the classical vibrational motion for each level $v$ from rotationless energies $G(v)$ and inertial rotational constants $B(v)$. The most commonly used procedures to extract $G(v)$ and $B(v)$ from the $\{E(v, J)\}$ set are the Dunham expansion and the near-dissociation (NDE) expansion, which are briefly recalled below. The former one describes accurately the system around its equilibrium internuclear distance, but does not yield a correct asymptotic behaviour. The latter extrapolates the representation towards the dissociation limit with good accuracy. In the set of experimental data for the $\{(v, J)\}$ energy levels (Fig. 6), a systematic energy shift due to temperature effects is expected [32], which can reach $\sim$ 100 MHz at 2 mK for the highest ($J = 8$) rotational level, but is negligible at the present level of accuracy for $J < 5$. This effect corresponds to the limit of the experimental resolution. Therefore the following analysis will be restricted to $J \leq 5$, but we have checked that the quality of the results is not significantly modified when including the highest $J$ levels.

### 4.1 Dunham procedure

In the initial work of Dunham [33] the energies $E(v, J)$ belonging to a single electronic state of a diatomic molecule may be written as the following expansion, so-called "Dunham-type":

$$E(v, J) = \sum_{l=0}^{\infty} \sum_{m=0}^{\infty} Y_{lm}(v + 1/2)^l [J(J + 1)]^m. \qquad (4.1)$$

The $Y_{lm}$ terms are known as the Dunham coefficients. Equation (4.1) can be recasted into:

$$E(v, J) = \sum_{m=0}^{\infty} K_m(v)[J(J + 1)]^m \qquad (4.2)$$

**Table 1.** Primary (Dunham-type) molecular parameters $Y_{lm}$ of the $0_g^-$ state of $Cs_2$ (Number of observed rovibrational transitions: 484 ($0 \leq J \leq 5$); r.m.s. of the deviations: 0.0015 $cm^{-1}$). All quantities are in $cm^{-1}$ except $R_e$ (in Å). One standard deviation is quoted in parentheses for each parameter. $R_e$ is calculated from $B_e = Y_{01} = h/(8\pi^2 c\mu R_e^2)$.

| | | |
|---|---|---|
| $Y_{10}$ | 1.785 567 4 | (0.000 060) |
| $Y_{20} \times 10$ | −0.138 539 4 | (0.000 051) |
| $Y_{30} \times 10^4$ | 0.266 206 0 | (0.001 3) |
| $Y_{50} \times 10^8$ | 0.373 689 8 | (0.005 2) |
| $Y_{60} \times 10^{10}$ | −0.490 602 9 | (0.008 8) |
| $Y_{70} \times 10^{12}$ | 0.257 264 5 | (0.005 8) |
| $Y_{80} \times 10^{15}$ | −0.518 871 5 | (0.001 4) |
| $Y_{01} \times 10^2$ | 0.166 726 7 | (0.001 4) |
| $Y_{11} \times 10^4$ | −0.157 617 6 | (0.003 6) |
| $R_e$ | 12.357 8 Å | (0.051 9) |

with

$$K_m(v) = \sum_{l=0}^{\infty} Y_{lm}(v + 1/2)^l. \qquad (4.3)$$

In this expansion, the $m = 0$ term $K_0(v)$ is identified as the rotationless vibrational energy $G(v)$, and the $m = 1$ term $K_1(v)$ as the inertial rotational constant $B(v)$. The following constants with $m = 2, 3, \ldots$, $K_2(v) \equiv -D(v)$, $K_3(v) \equiv H(v)$, ... are the centrifugal distortion constants. The first Dunham coefficients $Y_{10} \equiv \omega_e$ and $Y_{01} \equiv B_e$ are easily interpreted respectively as the harmonic and rotational constant at equilibrium. The equilibrium distance $R_e$ is extracted through the relation $B_e = h/(8\pi^2 c\mu R_e^2)$, where $\mu$ is the reduced mass of the system ($\mu$=121 135.828 a.u. for $^{133}Cs_2$ [34]).

The initial data set for the Dunham procedure are the wavenumbers of the quasi-resonant transitions connecting the initial continuum state of the two cold atoms and the rovibrational levels in the $0_g^-(v, J)$ presently studied. Energies may then be referred to the lowest ($v = 0, J = 0$) level by subtracting the corresponding transition wavenumber. A Dunham fit, according to equation (4.1) of the experimental data set represented in Figure 6 gives the Dunham coefficients quoted in Table 1. With these coefficients the initial experimental data set $\{E(v, J)\}$ are reproduced to within 0.0015 $cm^{-1}$. Due to the low values of the observed $J$ numbers, the contribution to energy of the higher order distortion parameters is found negligible. The equilibrium internuclear distance $R_e = 12.36 \pm 0.05$ Å $\equiv 23.36 \pm 0.10 a_0$ ($a_0 = 0.529\,177\,2$ Å), is slightly shorter than previous prediction ($R_e = 24.56 a_0$, [30]) based on asymptotic calculations. We will further discuss this point in Section 5.

The last spectral line included has a detuning of about 0.4 $cm^{-1}$. The Dunham representation offers only a poor extrapolation of the energy terms towards the dissociation limit, which can be improved by Near-Dissociation Expansion theory described below.

### 4.2 The near-dissociation expansion theory

The analysis of PA data near the dissociation energy aims at providing the long-range behaviour of the potential curve, which writes for $R \to \infty$:

$$V(R) = D - C_n/R^n \tag{4.4}$$

where $D$ is the energy at the molecular dissociation limit and $C_n$ the leading long-range coefficient ($n = 3$ for dipole-dipole interaction in the present case). Depending upon the choice for the energy origin, $D$ can be either zero (origin at the dissociation limit) or the value of the well depth $D_e$ (origin at the minimum of the studied potential well). From equation (4.4), LeRoy and Bernstein [35] and Stwalley [36,37] (see also Ref. [38]) derived the near dissociation limiting behavior $K_m^\infty(v)$ of the quantities $K_m(v)$ in equation (4.3). For the vibrational terms ($m = 0$):

$$G^\infty(v) \equiv K_0^\infty(v) = D_e - X_0(n)(v_D - v)^{2n/(n-2)} \tag{4.5}$$

and for the rotational constant ($m = 1$):

$$B^\infty(v) \equiv K_1^\infty(v) = X_1(n)(v_D - v)^{[2n/(n-2)-2]}. \tag{4.6}$$

More generally, if $m > 0$, the distortion terms are written:

$$K_m^\infty(v) = X_m(n)(v_D - v)^{[2n/(n-2)-2m]}. \tag{4.7}$$

In the above equations, $v_D$ is the effective vibrational (non-integer) index at the dissociation energy and,

$$X_m(n) = \bar{X_m}(n)/\left[\mu^n(C_n^2)\right]^{1/(n-2)} \tag{4.8}$$

where the quantities $\bar{X_m}(n)$ are known tabulated constants[1] [39]. In the particular case of the $Cs_2$ $0_g^-$ state dissociating into the limit Cs ($6s\ ^2S_{1/2}$)+Cs ($6p\ ^2P_{3/2}$), we have (setting $n = 3$):

$$X_m(3) = \bar{X_m}(3)/\mu^3 C_3^2. \tag{4.9}$$

However, equations (4.4) and following are valid only for very large internuclear distances (or for levels very close to the dissociation limit), and when hyperfine structure and retardation effects are neglected. Moreover, further $R^{-n}$ terms beyond the dipole-dipole approximation in the expansion (4.4) are required to reproduce larger parts of PA spectra [40]. Such detailed long-range analysis of PA data have been recently performed for the $0_g^-$ state in $Na_2$ [11] and $K_2$ [12], yielding an accurate value of the leading coefficient $C_3$ in equation (4.4), directly related to the lifetime of the first $P_{3/2}$ atomic level. In the present case this cannot easily be done as, in contrast with lighter alkali dimers, the $0_g^-$ state in $Cs_2$ is no longer a pure long-range molecular state (see Sect. 5), and the hyperfine structure is much larger.

[1] In the computer program we have used the values $\bar{X_0}(3) = 36\,409.62$ and $\bar{X_1}(3) = 60\,221.029$ when energies are in $cm^{-1}$, distances in Å and mass in a.m.u.

Instead, we follow the procedure which has been successfully used for the $Rb_2$ $0_g^-$ state [41]. The near dissociation analysis is combined with the Dunham approach within the Near-Dissociation Expansion (NDE) theory developed by Beckel and co-workers [42,43] and LeRoy and co-workers [44,45], in order to provide a description of the entire spectra. As the Dunham type expansion does not have the correct limiting behavior and cannot be reliably applied to vibrational levels close to the dissociation limit, the near-dissociation expansion (NDE) expressions ensure the correct $K_m(v)$ behavior both for near equilibrium and for near dissociation spectral data by correcting the vibrational energy at infinity with a Padé approximant $[L/M]$:

$$\begin{aligned} G(v) \equiv K_0(v) &= K_0^\infty(v)[L/M] \\ &= D_e - X_0(n)(v_D - v)^{2n/(n-2)}[L/M] \end{aligned} \tag{4.10}$$

where $[L/M]$, termed "outer" Padé expression, represent the ratio of two polynomials $\mathcal{P}_L$ and $\mathcal{Q}_M$ depending upon the variable $z = (v_D - v)^\gamma$:

$$\begin{aligned} \mathcal{P}_L &= 1 + \sum_{i=1}^{L} p_i z^{\alpha+i-1} \\ \mathcal{Q}_M &= 1 + \sum_{j=1}^{M} q_j z^{\beta+j-1}. \end{aligned} \tag{4.11}$$

Several fits have been performed to determine the value of the exponents $\alpha$, $\beta$, $\gamma$, $L$ and $M$, and we choose the one which ensures the best compromise between the accuracy and the compactness of the representation of the $\{E(v, J)\}$ set.

The other molecular parameters (with $m > 0$) are usually corrected by an exponential expansion of order $N$:

$$K_m(v) = K_m^\infty(v) \exp\left[\sum_{l=1}^{N} s_l (v_D - v)^l\right]. \tag{4.12}$$

Even though the parameters of such expansions have no direct physical meaning, these analytical continuations (Eqs. (4.10, 4.12)) of long-range representations (Eqs. (4.5–4.7)) have been shown [38,44,45] to be far better for extrapolation towards high $v$ values than simple Dunham-type expressions (Eqs. (4.2, 4.3)).

Another type of analytical long-range analysis is possible as for example in the accurate study of the long-range $0_u^+$ potential in $Li_2$ by Martin *et al.* [40]. The authors use higher order terms in the multipolar expansion of the potential (Eq. (4.4)), in order to extract the corresponding long-range parameters $C_n$ and the asymptotic form of the exchange energy. Our present study is concentrated onto the representation of the part of the potential curve covered by all the observed lines, by mixing in equation (4.10) the long-range behavior of the potential (a single $C_n$ coefficient) and additional parameters (in the $[L/M]$ expression).

The NDE analysis implies non-linear fits and does not have a unique solution. Here the input are the $G(v)$ and

**Table 2.** Parameters in the NDE fits of the $G(v)$ energy values. The nature $[L/M]$ of the outer Padé expressions is indicated for all fits, and coefficients given for fit $F_2$ as an example. The dissociation limit $D_e$ is evaluated from the bottom of the potential energy curve. The second order correction $Y_{00} = -0.0004$ cm$^{-1}$ has been included in $D_e$. The displayed value of $C_3$ is fixed in the $F_2$ fit to the theoretical value deduced from [30]. In the fit $F_3$, the $D_e$ value is fixed to the value of the $F_2$ fit.

| | | |
|---|---|---|
| $F_1$ | $v_D$ | 218.555(195) |
| [7/0] | $D_e$ | 77.957(3) |
| | $C_3$ | 11.616(50) a.u. $\equiv$ 377 804 cm$^{-1}$Å$^3$ |
| $F_2$ | $v_D$ | 214.639(130) |
| | $D_e$ | 77.928(4) |
| | $C_3$ | 10.47 a.u. $\equiv$ 340 513 cm$^{-1}$Å$^3$ |
| [2/2] | $p_1 \times 10^5$ | −1.147 468 293 |
| | $p_2 \times 10^8$ | 3.525 611 548 |
| | $q_1 \times 10^5$ | −1.761 471 370 |
| | $q_2 \times 10^8$ | 7.285 783 887 |
| | $X_0(3) \times 10^{11}$ | 0.107 007 8979 cm$^{-1}$ |
| $F_3$ | $v_D$ | 213.685(535) |
| | $D_e$ | 77.94 |
| | $C_3$ | 9.84(10) a.u. $\equiv$ 320 122(3000) cm$^{-1}$Å$^3$ |
| [1/0] | $p_1 \times 10^6$ | 1.1(1) |

**Table 3.** Parameters in the exponential NDE fit of the $B(v)$ rotational constants. The parameters $C_3$ and $v_D$ are constrained to the values given in Table 2 for the fit "$F_2$".

| | |
|---|---|
| $s_1$ | − 0.418 073 790 |
| $s_2 \times 10$ | 0.107 456 229 |
| $s_3 \times 10^3$ | − 0.110 050 347 |
| $s_4 \times 10^6$ | 0.567 155 470 |
| $s_5 \times 10^8$ | − 0.145 733 391 |
| $s_6 \times 10^{11}$ | 0.150 049 475 |
| $X_1(3) \times 10^{11}$ | 0.176 987 8010 |

$B(v)$ values resulting from the Dunham procedure. The full NDE analysis, summarized in Table 2 was conducted as follows.

1. A first fit "$F_1$" of all the energies $G(v)$ is performed [46], requiring quite high values of the exponents: $\alpha = 2$, $\beta = 2$, $\gamma = 6$, with a [7/0] "outer" Padé expression. Equation (4.10) has not a very compact form in this case. The converged long-range parameters are then: $v_D = 218.5(2)$, $D_e = 77.957(3)$ cm$^{-1}$ and $C_3 = 11.61(5)$ a.u. (or $377(2)\times10^3$ cm$^{-1}$Å$^3$). The entire set of observed $E(v, J)$ values is then represented with a standard deviation of 0.002 cm$^{-1}$. The long range parameter $v_D$ predicts more than 210 levels in the well, and the well depth is found slightly larger than the value $D_e = 75.55$ cm$^{-1}$ deduced from the asymptotic calculations of reference [30]. Moreover, the fitted parameter $C_3$ also differs noticeably from the value deduced from the same work ($C_3 = 10.47$ a.u. [30]), or from the one derived from precise atomic lifetime measurements ($C_3 = 10.1$ a.u. [47]). These discrepancies will be discussed in more details in Section 5. It is worthwhile to remark that a similar NDE analysis has been performed recently [41] for the $0_g^-(5s\ ^2S_{1/2} + 5p\ ^2P_{3/2})$ of $Rb_2$, yielding a fitted $C_3$ parameter in good agreement with the value obtained by asymptotic calculations.
2. Next, a further fit "$F_2$" of the energies $G(v)$ is performed with the constraint $C_3 = 10.47$ a.u.: a more compact expression is obtained, with $\alpha = 2$, $\beta = 2$, $\gamma = 1$, and a [2/2] "outer" Padé expression. The standard deviation on $E(v, J)$ values remains of the order of the experimental uncertainties (0.0031 cm$^{-1}$). The well depth and the limiting vibrational quantum number are only slightly modified.
3. According to our asymptotic calculations of the hyperfine structure, the $R^{-3}$ long-range behaviour of the $0_g^-$ state is expected to be strongly perturbed by the hyperfine structure, for detunings smaller than 3 cm$^{-1}$. Then in a third fit "$F_3$", the set of $G(v)$ data is limited to $70 \leq v \leq 100$, *i.e.* to a range where the $R^{-3}$ behaviour is expected to be correct (the contributions of higher order terms are indeed negligible). The parameter $D_e$ in equation (4.10) is held to the value given by the $F_2$ fit. As seen in Table 2, the [1/0] resulting Padé expression, with $\alpha = 2$, $\beta = 2$, $\gamma = 1$, is even more compact than from the "$F_2$" fit: a single parameter is required, which modifies only slightly the Leroy-Bernstein law of equation (4.5). But the fitted value of the parameter $C_3 = 9.84(10)$ a.u. is now 3% smaller than the one derived from atomic lifetime measurement, and 6% smaller than the theoretical value $C_3 = 10.47$ a.u. of reference [29].
   We can see that the $G(v)$ are well extrapolated towards the dissociation limit by the NDE procedure, as the potential depth and the fractional vibrational quantum numbers are very close over all the performed fits, and the standard deviation remains small. However, there is no fully satisfying solution for the extraction of the long-range parameter $C_3$ of the $0_g^-$ state. This is due to the combined effect of the large hyperfine structure, and of the particular short-range shape of the potential curve, as demonstrated in Section 5.
4. In the fit of the rotational constants $B(v)$, the $v_D$, $D_e$ parameters are constrained to the values obtained in the $F_2$ fit (with $C_3 = 10.47$ a.u.), choosing $N = 6$. It is worth to notice that the experimentally observed rotational structures are not resolved beyond $v = 74$. So we benefit of the powerful features of the NDE algorithm in extrapolating unobserved $B(v)$ values for $75 < v \leq 132$ according to equation (4.12). The final converged parameters are listed in Table 3, reproducing the observed rotational structure accurately, the largest discrepancy being of about 0.1% for the $v = 74$ level.

### 4.3 The Rydberg-Klein-Rees method for potential determination

The classical turning points $R_-(v)$ and $R_+(v)$ are determined from the Klein integrals:

$$R_+(v) - R_-(v) = \frac{2\hbar}{\sqrt{2\mu}} \int_{v_{min}}^{v} \frac{dv'}{[G(v) - G(v')]^{1/2}}$$
$$\frac{1}{R_-(v)} - \frac{1}{R_+(v)} = \frac{\hbar}{2\pi\sqrt{2\mu}} \int_{v_{min}}^{v} \frac{B(v')dv'}{[G(v) - G(v')]^{1/2}} \quad (4.13)$$

where $R_-(v)$ and $R_+(v)$ are the inner and outer turning points for a classical motion with energy $G(v)$, and with rotational constant $B(v)$. The lower bound $v_{min}$ is the extrapolated value of the (non-integer) vibrational quantum number at the potential minimum (equal to $-0.5000(2)$ here).

The NDE algorithm offers a physically more reliable representation of the $G(v)$ and $B(v)$ quantities, especially near the dissociation limit, because equations (4.5–4.7) have explicitly the near-limit behavior in the long-range region. The final $G(v)$ and $B(v)$ sets, derived from the parameters of the fit "$F_2$" (see Tabs. 2, 3), are taken as the input for the RKR calculations [48]. It is worth to notice that, as very low $J$ values levels are observed, the iterative procedure used by Ji *et al.* [38] to take account of the influence of higher order rotational distortion parameters $D(v)$, $H(v), \ldots$ is not necessary since their energy contribution is completely negligible in the present case. An inner wall "wiggling" due to the increasing spacing between successive $R_+(v)$ for the highest vibrational levels occurs starting from $v = 60$ (inner turning point at $R_- = 8.908$ Å). Therefore, as suggested by LeRoy, the inner part of the potential curve is corrected for lower $R$. In the present case, for all levels above $v = 50$, the position of the inner turning points are smoothed assuming an exponential variation of the repulsive inner potential wall:

$$V(R_-)(\mathrm{cm}^{-1}) = -2.9842 + 0.1497098 \times 10^5 \exp[-0.6084714 R_-(\text{Å})] \quad (4.14)$$

builded from $R_-(48)$, $R_-(49)$, $R_-(50)$ data points. Such an extrapolation ensures a proper representation of the measured $B_v$ between $v = 50$ and $v = 74$.

The RKR turning points up to the last observed vibrational level $v = 132$ are listed in Table 4. The final RKR potential energy curve is plotted in Figure 7. The inset shows that the fit "$F_1$" tends to provide an inner wall slightly steeper than from the fit "$F_2$", while no visible change is obtained in the asymptotic region.

The quality of this potential is finally checked by solving the radial Schrödinger equation and computing the eigenvalues and distortion constants [49]. The difference with the experimentally observed term values are lower than 0.010 $\mathrm{cm}^{-1}$ up to $v = 74$. The rotational constant $B(v)$ is recalculated within an accuracy better than 0.1%. The positions of the lines in the spectra in terms of red

**Table 4.** The output inner and outer turning points of the RKR analysis using parameters of the fit "$F_2$" in Table 2. The origin of energies is taken at the bottom of the well. The experimental detuning $\delta^{exp}(v)$ can be deduced according to the formula: $\delta^{exp}(v) = \delta^{exp}(0) + (G(v) - G(0))$, where $\delta^{exp}(0) = -77.129$ $\mathrm{cm}^{-1}$ is the measured detuning of the $(v = 0, J = 0)$ level. Beyond $v = 74$ (horizontal line), no rotational structure is resolved.

| $v$ | $G(v)\,(\mathrm{cm}^{-1})$ | $B(v)\,(\mathrm{cm}^{-1})$ | $R_-(v)\,(\text{Å})$ | $R^+(v)\,(\text{Å})$ |
|---|---|---|---|---|
| 0 | 0.890 | 0.00166 | 11.830 | 12.899 |
| 1 | 2.649 | 0.00164 | 11.496 | 13.360 |
| 2 | 4.380 | 0.00163 | 11.281 | 13.703 |
| 3 | 6.085 | 0.00161 | 11.114 | 13.999 |
| 4 | 7.761 | 0.00160 | 10.975 | 14.269 |
| 5 | 9.411 | 0.00158 | 10.856 | 14.522 |
| 6 | 11.033 | 0.00156 | 10.749 | 14.762 |
| 7 | 12.629 | 0.00155 | 10.654 | 14.994 |
| 8 | 14.198 | 0.00153 | 10.567 | 15.220 |
| 9 | 15.741 | 0.00152 | 10.486 | 15.440 |
| 10 | 17.258 | 0.00150 | 10.412 | 15.657 |
| 11 | 18.748 | 0.00149 | 10.342 | 15.871 |
| 12 | 20.213 | 0.00147 | 10.276 | 16.082 |
| 13 | 21.652 | 0.00145 | 10.215 | 16.293 |
| 14 | 23.065 | 0.00144 | 10.156 | 16.502 |
| 15 | 24.454 | 0.00142 | 10.101 | 16.710 |
| 16 | 25.817 | 0.00141 | 10.048 | 16.918 |
| 17 | 27.156 | 0.00139 | 9.998 | 17.127 |
| 18 | 28.469 | 0.00138 | 9.950 | 17.335 |
| 19 | 29.759 | 0.00136 | 9.903 | 17.544 |
| 20 | 31.024 | 0.00134 | 9.859 | 17.754 |
| 21 | 32.265 | 0.00133 | 9.816 | 17.965 |
| 22 | 33.483 | 0.00131 | 9.775 | 18.178 |
| 23 | 34.677 | 0.00130 | 9.736 | 18.391 |
| 24 | 35.847 | 0.00128 | 9.698 | 18.606 |
| 25 | 36.995 | 0.00127 | 9.661 | 18.823 |
| 26 | 38.119 | 0.00125 | 9.625 | 19.042 |
| 27 | 39.221 | 0.00123 | 9.590 | 19.262 |
| 28 | 40.301 | 0.00122 | 9.557 | 19.485 |
| 29 | 41.358 | 0.00120 | 9.525 | 19.710 |
| 30 | 42.394 | 0.00119 | 9.493 | 19.938 |
| 31 | 43.408 | 0.00117 | 9.462 | 20.168 |
| 32 | 44.400 | 0.00115 | 9.433 | 20.401 |
| 33 | 45.371 | 0.00114 | 9.404 | 20.637 |
| 34 | 46.321 | 0.00112 | 9.376 | 20.875 |
| 35 | 47.251 | 0.00111 | 9.348 | 21.117 |
| 36 | 48.160 | 0.00109 | 9.322 | 21.362 |
| 37 | 49.049 | 0.00108 | 9.296 | 21.610 |
| 38 | 49.917 | 0.00106 | 9.271 | 21.862 |
| 39 | 50.767 | 0.00104 | 9.247 | 22.117 |
| 40 | 51.596 | 0.00103 | 9.223 | 22.376 |

**Table 4.** continued.

| $v$ | $G(v)\,(\mathrm{cm}^{-1})$ | $B(v)\,(\mathrm{cm}^{-1})$ | $R_-(v)\,(\text{Å})$ | $R^+(v)\,(\text{Å})$ |
|---|---|---|---|---|
| 41 | 52.407 | 0.00101 | 9.200 | 22.639 |
| 42 | 53.198 | 0.00100 | 9.177 | 22.906 |
| 43 | 53.971 | 0.00098 | 9.156 | 23.177 |
| 44 | 54.726 | 0.00097 | 9.134 | 23.452 |
| 45 | 55.462 | 0.00095 | 9.114 | 23.732 |
| 46 | 56.181 | 0.00093 | 9.094 | 24.017 |
| 47 | 56.882 | 0.00092 | 9.075 | 24.306 |
| 48 | 57.565 | 0.00090 | 9.056 | 24.600 |
| 49 | 58.232 | 0.00089 | 9.038 | 24.899 |
| 50 | 58.881 | 0.00087 | 9.021 | 25.203 |
| 51 | 59.515 | 0.00086 | 9.004 | 25.513 |
| 52 | 60.131 | 0.00084 | 8.988 | 25.829 |
| 53 | 60.732 | 0.00082 | 8.972 | 26.150 |
| 54 | 61.317 | 0.00081 | 8.957 | 26.476 |
| 55 | 61.887 | 0.00079 | 8.943 | 26.809 |
| 56 | 62.441 | 0.00078 | 8.929 | 27.148 |
| 57 | 62.980 | 0.00076 | 8.915 | 27.493 |
| 58 | 63.505 | 0.00075 | 8.902 | 27.845 |
| 59 | 64.015 | 0.00073 | 8.890 | 28.203 |
| 60 | 64.511 | 0.00071 | 8.878 | 28.568 |
| 61 | 64.993 | 0.00070 | 8.866 | 28.941 |
| 62 | 65.462 | 0.00068 | 8.855 | 29.320 |
| 63 | 65.917 | 0.00067 | 8.844 | 29.707 |
| 64 | 66.359 | 0.00065 | 8.833 | 30.101 |
| 65 | 66.788 | 0.00063 | 8.823 | 30.503 |
| 66 | 67.204 | 0.00062 | 8.813 | 30.913 |
| 67 | 67.608 | 0.00060 | 8.804 | 31.332 |
| 68 | 68.000 | 0.00059 | 8.795 | 31.759 |
| 69 | 68.380 | 0.00057 | 8.786 | 32.195 |
| 70 | 68.749 | 0.00056 | 8.778 | 32.639 |
| 71 | 69.106 | 0.00054 | 8.769 | 33.093 |
| 72 | 69.452 | 0.00052 | 8.762 | 33.557 |
| 73 | 69.787 | 0.00051 | 8.754 | 34.030 |
| 74 | 70.112 | 0.00049 | 8.747 | 34.513 |
| 75 | 70.426 | 0.00048 | 8.740 | 35.006 |
| 76 | 70.730 | 0.00046 | 8.733 | 35.511 |
| 77 | 71.024 | 0.00045 | 8.726 | 36.026 |
| 78 | 71.309 | 0.00043 | 8.720 | 36.552 |
| 79 | 71.583 | 0.00042 | 8.714 | 37.091 |
| 80 | 71.849 | 0.00040 | 8.708 | 37.641 |
| 81 | 72.106 | 0.00039 | 8.702 | 38.203 |
| 82 | 72.354 | 0.00037 | 8.697 | 38.779 |
| 83 | 72.593 | 0.00036 | 8.692 | 39.367 |
| 84 | 72.824 | 0.00035 | 8.687 | 39.969 |
| 85 | 73.047 | 0.00033 | 8.682 | 40.585 |
| 86 | 73.262 | 0.00032 | 8.677 | 41.215 |

**Table 4.** continued.

| $v$ | $G(v)\,(\mathrm{cm}^{-1})$ | $B(v)\,(\mathrm{cm}^{-1})$ | $R_-(v)\,(\text{Å})$ | $R^+(v)\,(\text{Å})$ |
|---|---|---|---|---|
| 87 | 73.469 | 0.00030 | 8.673 | 41.860 |
| 88 | 73.669 | 0.00029 | 8.669 | 42.521 |
| 89 | 73.862 | 0.00028 | 8.664 | 43.197 |
| 90 | 74.047 | 0.00027 | 8.660 | 43.890 |
| 91 | 74.225 | 0.00025 | 8.657 | 44.600 |
| 92 | 74.397 | 0.00024 | 8.653 | 45.327 |
| 93 | 74.562 | 0.00023 | 8.650 | 46.072 |
| 94 | 74.721 | 0.00022 | 8.646 | 46.835 |
| 95 | 74.874 | 0.00021 | 8.643 | 47.618 |
| 96 | 75.021 | 0.00019 | 8.640 | 48.421 |
| 97 | 75.162 | 0.00018 | 8.637 | 49.244 |
| 98 | 75.297 | 0.00017 | 8.634 | 50.089 |
| 99 | 75.427 | 0.00016 | 8.631 | 50.956 |
| 100 | 75.552 | 0.00015 | 8.629 | 51.845 |
| 101 | 75.671 | 0.00014 | 8.626 | 52.759 |
| 102 | 75.786 | 0.00014 | 8.624 | 53.696 |
| 103 | 75.895 | 0.00013 | 8.622 | 54.659 |
| 104 | 76.000 | 0.00012 | 8.619 | 55.649 |
| 105 | 76.101 | 0.00011 | 8.617 | 56.665 |
| 106 | 76.197 | 0.00010 | 8.615 | 57.710 |
| 107 | 76.289 | 0.00010 | 8.613 | 58.784 |
| 108 | 76.377 | 0.00009 | 8.612 | 59.889 |
| 109 | 76.461 | 0.00008 | 8.610 | 61.025 |
| 110 | 76.542 | 0.00008 | 8.608 | 62.194 |
| 111 | 76.618 | 0.00007 | 8.607 | 63.396 |
| 112 | 76.692 | 0.00007 | 8.605 | 64.635 |
| 113 | 76.761 | 0.00006 | 8.604 | 65.910 |
| 114 | 76.828 | 0.00006 | 8.602 | 67.224 |
| 115 | 76.891 | 0.00005 | 8.601 | 68.577 |
| 116 | 76.951 | 0.00005 | 8.600 | 69.972 |
| 117 | 77.009 | 0.00004 | 8.598 | 71.410 |
| 118 | 77.063 | 0.00004 | 8.597 | 72.892 |
| 119 | 77.115 | 0.00004 | 8.596 | 74.422 |
| 120 | 77.164 | 0.00003 | 8.595 | 76.001 |
| 121 | 77.211 | 0.00003 | 8.594 | 77.630 |
| 122 | 77.256 | 0.00003 | 8.593 | 79.313 |
| 123 | 77.298 | 0.00002 | 8.593 | 81.051 |
| 124 | 77.338 | 0.00002 | 8.592 | 82.847 |
| 125 | 77.375 | 0.00002 | 8.591 | 84.704 |
| 126 | 77.411 | 0.00002 | 8.590 | 86.624 |
| 127 | 77.445 | 0.00002 | 8.590 | 88.610 |
| 128 | 77.477 | 0.00001 | 8.589 | 90.666 |
| 129 | 77.507 | 0.00001 | 8.588 | 92.794 |
| 130 | 77.536 | 0.00001 | 8.588 | 94.998 |
| 131 | 77.562 | 0.00001 | 8.587 | 97.282 |
| 132 | 77.588 | 0.00001 | 8.587 | 99.650 |

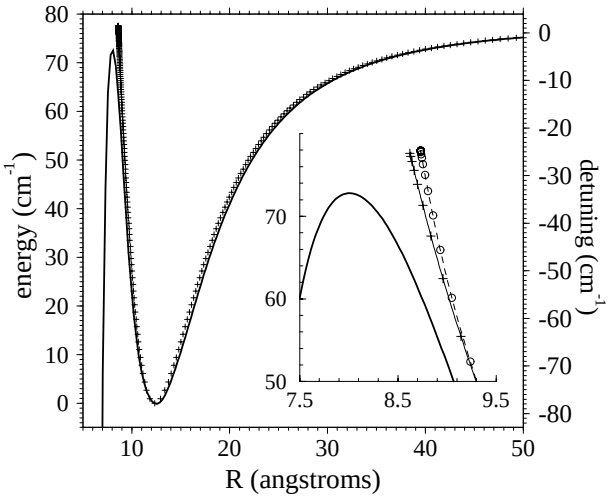


**Fig. 7.** The $Cs_2\, 0_g^-$ potential curve. Crosses: the RKR potential energy curve determined from the 133 vibrational and 75 rotational observed spectral data, with the fit "$F_2$". Full line: theoretical potential described in Section 5. Inset: blow-up of the short-range part of the curves, including also the RKR determination from the fit "$F_1$" (open circles).

detuning from the $^2S_{1/2}(F=4) \rightarrow\ ^2P_{3/2}(F'=5)$ transition (11 732.183 $cm^{-1}$) can be determined from Table 4, considering for instance the measured detuning of the $(v=0; J=0)$ level ($-77.129$ $cm^{-1}$). The dissociation limit of the RKR curve is lying 0.089(3) $cm^{-1}$ below the $^2S_{1/2}(F=4) +^2 P_{3/2}(F'=5)$ dissociation limit. This is not surprising, as no data concerning hyperfine structure, which dominates the spectrum for small detunings, are included in the RKR analysis.

## 5 Discussion; double-well structure and comparison with quantum chemistry determination of the $0_g^-$ potential curve

The previous model relies upon the fact that the observed series is belonging to a single isolated potential curve, unperturbed by other neighbouring electronic states. It is therefore valuable to compare the potential derived from experimental data with other theoretical models. In this section, we recall how asymptotic models explain the origin of the long-range wells in the $0_g^-(ns^2S_{1/2} + np^2P_{3/2})$ state in alkali dimers, and their evolution from light to heavy systems. We show that this model establishes clearly the existence of a double well shape of this curve for $Cs_2$. Quantum chemistry computations confirm this pattern, and their results are carefully compared to the RKR determination.

### 5.1 Asymptotic model: the particular behaviour of $Cs_2$

Since the pioneering work of Dashevskaya *et al.* [50], the shape of the long range adiabatic potential curves of the alkali dimers correlated to the first $ns\,^2S_{1/2} + np\,^2P_{1/2,3/2}$ asymptotes has been discussed in many papers [30,51–53]. From [50], it is clear that the sign and magnitude of the long range $R^{-3}$ dipole-dipole interaction depend upon the orientation of the two atomic dipoles relative to the internuclear axis and relative to each other. The relevant symmetry property, for the asymptotic Hund's case (a) molecular wavefunction obtained by antisymetrized combination of the two unperturbed atomic wavefunctions, is the exchange of excitation between the two atoms, leaving the core and electrons unchanged. It can be expressed as the product of the symmetry in exchange of the two electrons multiplied by the symmetry in exchange of the two cores

$$\pi = (-1)^S w \tag{5.1}$$

where $S$ is the (integer) electronic spin of the system, and $w = \pm 1$ for $g$ and $u$ symmetry respectively.

Once the fine structure is introduced in a perturbative treatment, the $0_g^-$ curves arise as a mixture of two antisymmetric states ($\pi = -1$), for each of which the two atomic dipoles are oriented in the same direction.

1. A $^3\Sigma_g^+$ state for which both dipoles are parallel to the molecular axis ($\rightarrow\rightarrow$) resulting into a potential $V_\Sigma(R)$ attractive in the asymptotic region ($R \rightarrow \infty$):

$$V_\Sigma(R) = -2\frac{C_3}{R^3} - \frac{C_6^\Sigma}{R^6} - \frac{C_8^\Sigma}{R^8} + \cdots \tag{5.2}$$

2. A $^3\Pi_g$ state for which both dipoles are perpendicular to the internuclear axis ($\uparrow\uparrow$), leading to a potential curve $V_\Pi(R)$) repulsive in the asymptotic region ($R \rightarrow \infty$):

$$V_\Pi(R) = \frac{C_3}{R^3} - \frac{C_6^\Pi}{R^6} - \frac{C_8^\Pi}{R^8} + \cdots \tag{5.3}$$

In both cases the $C_3$ constant is simply related to the atomic dipole transition moment, and hence to the lifetime of the $np$ atomic state by $C_3 = (e^2/4\pi\epsilon_0)|\langle ns|z|np\rangle|^2$.

The existence of the well in the adiabatic $0_g^-(np\,^2P_{3/2})$ potential curve dissociating into $(ns\,^2S_{1/2} + np\,^2P_{3/2})$ is linked to an avoided crossing with the flat $0_g^-(np\,^2P_{1/2})$ curve correlated to the $(ns\,^2S_{1/2} + np\,^2P_{1/2})$ dissociation limit. It is easy to estimate the position of this minimum in the framework of asymptotic calculations. A convenient choice consists in writing the effective spin-orbit Hamiltonian in the Hund's case (c) representation for the asymptotic molecular wavefunction, in which the atomic fine structure term, depending upon the fine structure constant $A$, is diagonal:

$$H^{so}(R) = \begin{pmatrix} \frac{A}{2} + \frac{2}{3}V_\Sigma(R) + \frac{1}{3}V_\Pi(R) & \frac{\sqrt{2}}{3}(V_\Sigma(R) - V_\Pi(R)) \\ \frac{\sqrt{2}}{3}(V_\Sigma(R) - V_\Pi(R)) & -A + \frac{1}{3}V_\Sigma(R) + \frac{2}{3}V_\Pi(R) \end{pmatrix}. \tag{5.4}$$

The upper diagonal element is attractive at large distances while the lower diagonal element corresponds to a flat curve. The $R$-dependent coupling is due to the difference between the two (Hund's case (a)) potentials $V_\Sigma(R)$ and $V_\Pi(R)$:

$$H_{12}^{so}(R) = \frac{\sqrt{2}}{3}(V_\Sigma(R) - V_\Pi(R)) = -\sqrt{2}\frac{C_3}{R^3} - \frac{\sqrt{2}}{3}\frac{C_6^\Pi - C_6^\Sigma}{R^6} - \frac{\sqrt{2}}{3}\frac{C_8^\Pi - C_8^\Sigma}{R^8} + \cdots \quad (5.5)$$

In a model considering only the leading $R^{-3}$ dipole dipole interaction and hence neglecting the $R^{-6}$ and $R^{-8}$ terms, the energy of the $0_g^-(ns\,^2S_{1/2} + np\,^2P_{3/2})$ curve is readily obtained after diagonalization the matrix in equation (5.4):

$$V(0_g^-(np\,^2P_{3/2})) = E(np\,^2P_{3/2}) - \frac{C_3}{R^3} + \frac{1}{2}x\left[\sqrt{1 + \frac{8}{x^2}\frac{(C_3)^2}{R^6}} - 1\right] \quad (5.6)$$

where $E_\infty(np\,^2P_{3/2})$ is the energy of the $(ns\,^2S_{1/2} + np\,^2P_{3/2})$ dissociation limit and $x = \Delta E_{fs} - C_3/R^3 = 3A/2 - C_3/R^3$ is the difference between the atomic fine structure splitting $\Delta E_{fs} = 3A/2$ and the dipole-dipole attractive interaction.

At large internuclear distances where the fine structure splitting is much larger than the dipole-dipole interaction ($x \simeq \Delta E_{fs}$), the upper curve is attractive:

$$V(0_g^-(np\,^2P_{3/2})) \simeq E_\infty(np\,^2P_{3/2}) - \frac{C_3}{R^3} + \frac{2(C_3)^2}{\Delta E_{fs} R^6}\cdot \quad (5.7)$$

The $R^{-6}$ correction is always comparable to the terms neglected in multipole expansion (Eqs. (5.2, 5.3)). As the internuclear distance is decreasing, the attractive dipole-dipole interaction and the fine structure splitting are comparable in magnitude ($x \simeq 0$), and we can write:

$$V(0_g^-(np\,^2P_{3/2})) \simeq E(np\,^2P_{3/2}) + (\sqrt{2} - 1)\frac{C_3}{R^3} \quad (5.8)$$

leading to a repulsive $R^{-3}$ branch. A minimum in the potential is generated at a distance which decreases rapidly from light to heavy atoms [52].

When the $R^{-6}$ and $R^{-8}$ terms of equations (5.2, 5.3) terms are considered, as the $C_6$ and $C_8$ coefficients are positive, they introduce an attractive contribution which tends to compensate the repulsive $R^{-3}$ behaviour. For $Na_2$ and $K_2$, the minimum occurs at very large distances ($\sim 72a_0$ and $\sim 52a_0$ respectively [52]) where the $R^{-6}$ and $R^{-8}$ terms can safely be neglected, so that the picture of a pure long range $R^{-3}$ potential well is indeed valid. In the case of heavier alkalis, due to the large value of the fine structure splitting, the minimum occurs in a region where the $R^{-6}$ and $R^{-8}$ terms should be introduced.

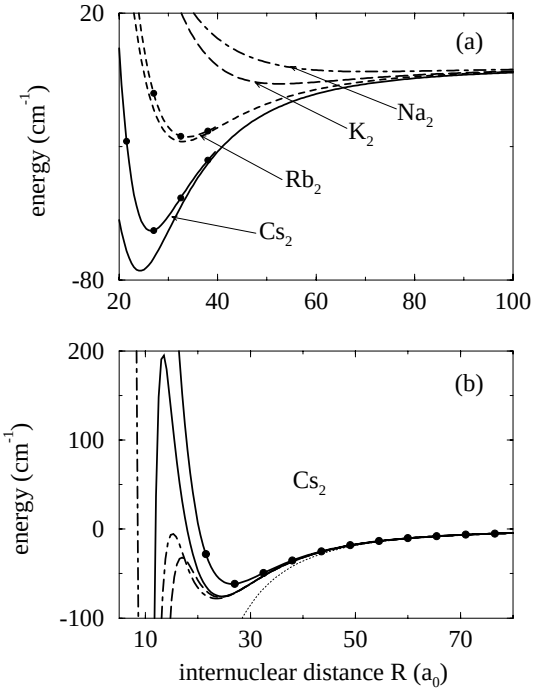


**Fig. 8.** (a) Long range well in the $0_g^-$ potential curve for the various alkali dimers, computed from multipolar expansion including $R^{-3}$, $R^{-6}$ and $R^{-8}$ terms. For $Rb_2$ and $Cs_2$, the curve obtained by including only the $R^{-3}$ term (closed circles) is differing markedly from the previous one, while no difference is visible for $Na_2$ and $K_2$ at the scale of the figure. (b) Details of the hump in the potential curve for the cesium dimer, from ab-initio calculations (dot-dashed line), or asymptotic calculations: including only the $R^{-3}$ term (full line with closed circles); including $R^{-3}$, $R^{-6}$ and $R^{-8}$ terms (full line); including also the asymptotic exchange energy (dashed line). The $-C_3/R^3$ potential is also indicated for illustration (dotted line).

This is manifested in Figure 8a, where we have used the long-range coefficients of Marinescu and Dalgarno [29]. In the case of cesium, the repulsive branch is located at an internuclear distances small enough to observe, when $R$ decreases, a compensation of the $R^{-3}$ repulsive term by the attractive $R^{-6}$ and $R^{-8}$ terms, yielding a qualitative explanation for the presence of a hump at $R \approx 15a_0$. We see in Figure 8b that once these terms are introduced in the expansion the hump becomes close to the *ab initio* estimation. In the case of rubidium, this simple model is indicating a huge barrier instead of a intermediate hump as is manifested in Figure 8a.

But, when we introduce a perturbative exchange correction [30] in the present model for $Cs_2$, the maximum of the hump is found above the asymptote and no longer below: however, the huge value of the exchange correction shows that a perturbative treatment is not justified, so that asymptotic calculations cannot be used for an accurate estimation of the barrier height between the two wells.

Therefore, asymptotic calculations predict a double-well structure of the $0_g^-(6s\,^2S_{1/2} + 6p\,^2P_{3/2})$ potential curve of $Cs_2$, which is unique among the alkali dimers.

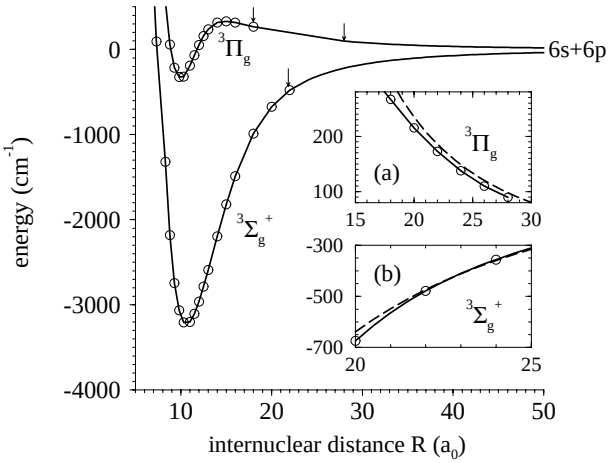


**Fig. 9.** The Hund's case (a) potential curves used in this work. The open circles indicates the *ab initio* calculated points [55,56]. Arrows show where the matching have been performed. Inset (a): blow up of the matching region of the *ab initio* $^3\Pi_g$ curve (full line) with the asymptotic curve (broken line). Inset (b): *idem* for the $^3\Sigma_g^+$ curve.

They also show that the height of the barrier is a very sensitive test for molecular potential calculations and estimation of exchange terms. We shall now compare with quantum chemistry results.

### 5.2 Computation of molecular potential curves

Quantum chemistry calculations, using pseudopotential techniques, have succeeded in obtaining an accuracy of a few tens of $cm^{-1}$ for the $Cs_2$ potential curves. Potential curves in the Hund's case (a) representation are available up to $20a_0$ in the recent calculations by Foucrault *et al.* [54], and up to $28a_0$ in those of Spiess and Meyer [55,56], with equivalent accuracy in their common range of internuclear distances. Because of their larger extension, we have considered the latter data for the potentials $V_\Sigma(R)$ and $V_\Pi(R)$ corresponding to the $(1)^3\Sigma_g^+$ and $(1)^3\Pi_g$ states. Then we have diagonalized the effective Hamiltonian matrix $H^{so}(R)$ of equation (5.4), where the atomic spin-orbit coupling parameter $A$ is chosen according to $3A/2 \equiv \Delta E_{fs} = 554.11$ $cm^{-1}$. This should be a reasonable assumption for the range of internuclear distances spanned by the $0_g^-$ external well.

At distances $R < 28a_0$, we tried to match the *ab initio* results of Spiess and Meyer [55,56] for the potential curves $V_\Sigma(R)$ and $V_\Pi(R)$, with the asymptotic curves computed using the $C_3$, $C_6$ and $C_8$ long-range coefficients of Marinescu and Dalgarno [29] and including the contribution of the asymptotic exchange energy as calculated in [30]. The $(1)^3\Sigma_g^+$ data sets are nicely matched at $22a_0$ (inset (b) in Fig. 9). In contrast, the *ab initio* determination and the asymptotic determination are providing two parallel $(1)^3\Pi_g$ curves between $22a_0$ and $28a_0$, separated each other by about 10 $cm^{-1}$ (inset (a) in Fig. 9). It is hard to say if such a difference may be attributed to some inaccuracy in the quantum chemistry calculations, or in the (non-relativistic) asymptotic calculations. This matching takes place right in the range of the minimum in the $0_g^-$ long-range well, which is expected around $23.4a_0$ (see Sect. 4.1). To avoid any discontinuity in the curves, we used the effective potential data for $R \leq 18a_0$, and the asymptotic data beyond $28a_0$: then a cubic spline procedure ensures a smooth matching within the $18a_0 < R < 28a_0$ zone.

### 5.3 The $0_g^-$ external well

The $0_g^-(6s\ ^2S_{1/2} + 6p\ ^2P_{3/2})$ resulting from the diagonalization of $H^{so}(R)$ is displayed in Figure 7, together with the RKR curve. It is compared with the asymptotic calculations in Figure 8b. The double well structure of the state is now clearly established, with the top of the barrier located at $15.2a_0$ and slightly below the dissociation limit (5.3 $cm^{-1}$). The agreement with the RKR curve is found good for the external well, both for the position of the minimum ($23.7a_0 = 12.53$ Å), and the well depth (78.2 $cm^{-1}$). This suggests that the assumed matching for $V_\Pi(R)$ is reasonable. The logarithmic derivative values of the energy terms $(1/G(v))(dG(v)/dv)$, are close to the RKR ones (Fig. 10a): it confirms that the overall shape of the potential, governing the splitting between the vibrational levels, is very similar in both methods. The good agreement with results of asymptotic calculations neglecting the exchange term (see Fig. 8b) may be fortuitous.

### 5.4 The potential barrier

The existence of a hump in the potential curve is clearly established both by asymptotic and by quantum chemistry calculations. However, the fit performed in Section 4.3 is not able to yield any information on the shape of the top of the barrier, as it considers only the levels of the external well.

The rotational constants computed from the *ab initio* curve are compared to experiment in Figure 10b, showing indeed a good agreement up to $v = 74$, as should be expected from the two set of potential curves. In the lack of experimental rotational constants $B(v)$ for the upper vibrational levels, the NDE theory yields an extrapolated curve with a slowly decreasing behaviour, related to the assumption of an exponential repulsive variation in the left part of the potential curve. In contrast, the effect of the barrier in the *ab initio* curve, located 5.3 $cm^{-1}$ below the dissociation limit is clearly reflected on the variation of the computed $B(v)$ around $v = 95$: the levels lying just above the top of the barrier display a sudden increase of their rotational constant, due to the large amplitude of the wavefunction in this region. For larger $v$, the rotational constant is again dominated by the long-range amplitude of the wavefunction, and $B(v)$ slowly decreases. However, in the experimental spectrum, only the giant rotational structure red-detuned by about 2 $cm^{-1}$ may be attributed

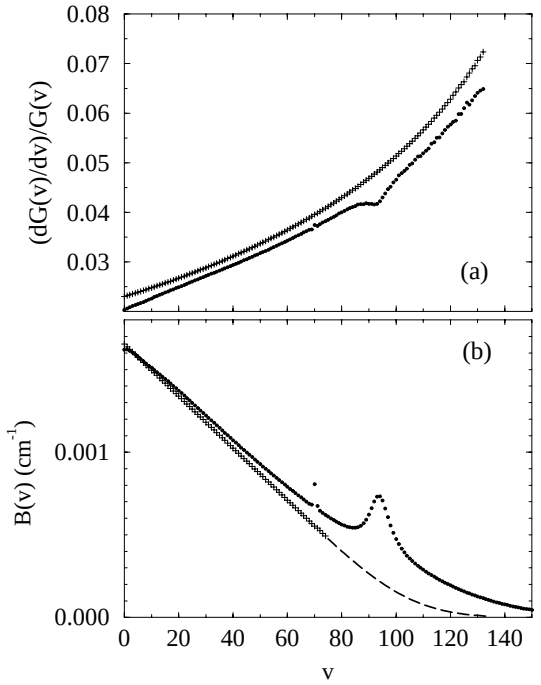


**Fig. 10.** The logarithmic derivative of the energy terms $(1/G(v))(dG(v)/dv)$ (a), and the rotational constants $B(v)$ (b), as a function of the vibrational quantum number $v$. Crosses: experimental values. Closed circles: $B(v)$ computed from theoretical potential of Section 5. In (a), the origin of energies is taken at the dissociation limit. In (b), values of $B(v)$ for levels with unresolved rotational structures and calculated using NDE theory ($74 \leq v \leq 132$) are indicated with a dashed line.

to a level with vibrational motion at distances typical of the internal well. The isolated jump in the computed $B(v)$ at $v = 70$ (red-detuned by 10.36 cm$^{-1}$) is due to a level of the external well, populated at long range by photoassociation and strongly coupled by tunneling through the barrier with a level of the internal well: this coupling gives rise to a giant resonance with a rotational constant of about 180 MHz, not represented here.

This comparison suggests that the top of the barrier should be located a few wavenumbers above the computed one, in order to account for the observation of tunneling towards a vibrational level of the internal well with a binding energy of 2 cm$^{-1}$ only. Tunneling effect through the barrier of the computed potential is also visible in Figure 10a, where a perturbation in the level splitting is expected at $v = 70$. Unfortunately, the experimental observation of this effect should occur for small detunings where the rotational constant cannot be determined. In this range of internulear distance (smaller than $15a_0$), neither the asymptotic exchange energy nor the *ab initio* calculations can be considered as more accurate than a few cm$^{-1}$. Complementary experimental data, for instance provided by Fourier Transform laser spectroscopy, are then needed to determine the shape of the internal well and to predict the position and the width of the resonant lines due to tunneling.

### 5.5 Long-range behavior of the potential

The NDE analysis has shown that it is not easy to find a satisfying value for the long-range parameter $C_3$. Moreover, beyond $50a_0$, the theoretical potential curve is not exactly following the RKR curve. At $50a_0$, for both the $V_\Sigma(R)$ and $V_\Pi(R)$ curves, the $C_6/R^6$ term accounts for less than 1% of the energy, the $C_8/R^8$ term for less than 0.1%, the exchange term being negligible. Then the theoretical curve is described with a good approximation by the expected inverse power law $-C_3^{eff}/R^3$, with $C_3^{eff}$ =10.47 a.u. constant to better than 1%. But in the same range, the $C_3^{RKR}(R)$ coefficient – deduced from the RKR curve by multiplying the potential energy by $R^3$ – varies from 5.5 a.u. at $50a_0$ to 11.3 a.u. at the dissociation limit, even if the $C_3$ coefficient in the fit "$F_2$" of the energies is kept constant at the theoretical value 10.47 a.u. This is due to the combined effect of the large hyperfine structure and of the particular double-well shape of the $0_g^-$ potential curve. A similar variation of the $C_3^{RKR}(R)$ coefficient is found in the RKR analysis of the $0_g^-$ state in $Rb_2$ [41]. This may be due to the fact that in the upper part of the fitted curve, the internal wall is extrapolated by a repulsive exponential term whereas a power law term seems more appropriate (see Sect. 5.1). For the $Rb_2(0_g^-)$ pure long-range curve, a $R^{-3}$ repulsive behavior of the inner branch should be expected; for the $Cs_2(0_g^-)$ curve, the left part of its external well is also strongly influenced by the attractive $-C_6/R^6$ and $-C_8/R^8$ terms, and by the exchange term.

## 6 Conclusion

Following our recent work reporting the first photoassociation spectroscopy experiment in $Cs_2$ [8], we have presented the spectroscopy of the $0_g^-(6s\,^2S_{1/2}+6p\,^2P_{3/2})$ long-range electronic state in $Cs_2$. We have discussed how an accurate potential can be fitted to the experimental data, representing 99.6% of the depth of potential well. The spectrum of the $1_u(6s\,^2S_{1/2}+6p\,^2P_{3/2})$ long-range $Cs_2$ electronic state has also been observed for the first time.

The photoassociation process in $Cs_2$ is very interesting because the $0_g^-$ rovibrational level may decay by spontaneous emission towards the lowest triplet state $a^3\Sigma_u^+$, leading to the formation of translationally cold molecules. We have also demonstrated the possibility to create cold molecules in their singlet ground state $X^1\Sigma_g^+$ by photoassociation of the $1_u\,(6s\,^2S_{1/2}+6p\,^2P_{3/2})$ long-range state. These results are promising for future developments in the field of cold molecules. The mechanism for the creation of long-lived molecules is attributed to spontaneous emission at a Condon point located at intermediate internuclear distances. In the case of the $0_g^-$ excitation, this Condon point is related to a double well structure in the potential curve. Moreover, a precise knowledge of the position of the classical outer turning point associated to the excited ro-vibrational levels is crucial for the determination of the scattering length. These considerations have been

an important motivation for the present determination of an accurate $0_g^-$ potential.

In order to reach this objective, we first have reported experimental results on a high resolution spectrum of the $Cs_2$ ($0_g^-$) long-range electronic state. Vibrational levels of the external well have been assigned from $v = 0$ up to $v = 132$, *i.e.* $\sim 0.3\ cm^{-1}$ below the dissociation limit $6s\ ^2S_{1/2} + 6p\ ^2P_{3/2}$. The rotational structure up to $J = 8$ is well resolved for levels below $v = 74$. Moreover, a vibrational series has been assigned to the $1_u$ electronic state. Finally, three isolated structures have been observed: two of them exhibit a huge rotational constant, probably associated with vibrational levels of the $0_g^-$ inner well.

The RKR potential energy curve has been constructed from the $0_g^-$ vibrational and rotational observed data up to $v = 74$. Accurate determination of the inner and outer turning points of the classical vibrational motion have been reported, with a 1% accuracy. As the rotational structure is not resolved beyond $v = 74$ in the experiment, the rotational constants were extrapolated using the NDE theory of Le Roy and co-workers. The NDE fitting of the energies cannot provide a converged value for the $C_3$ asymptotic parameter which varies by $\pm 10\%$ according to the performed fit. The long-range behavior of the RKR potential differs from the expected $-C_3/R^3$ asymptotic law, preventing a reliable determination of the radiative lifetime of the $6p\ ^2P_{3/2}$ atomic level, in contrast already performed for $Na_2$ and $K_2$ [9,12]. The RKR curve is probably less precise above the $v = 74$ level (or outside the $[16a_0, 65a_0]$ range of internuclear distances) as no experimental rotational constants are measured. In the fitting procedure, we have constrained the evolution of the inner classical turning point for $v > 50$, by assuming an exponential law for the repulsive branch of the potential. A better adapted variation of the repulsive branch could be introduced in the fitting procedure, and could lead to a shift of the outer classical turning point possibly as large as 1 Å for the highest vibrational levels.

The existence of a barrier can be qualitatively predicted at distances $R \sim 15a_0$ from asymptotic calculations, and we have shown that the inner branch of the external well has a smooth repulsive behavior dominated by a $R^{-3}$ term. We have also discussed the reliability of a potential curve determined from *ab initio* calculations matched around $R \sim 25a_0$ with asymptotic calculations at large distances: there is a good agreement (within $0.5\ cm^{-1}$) for the prediction of the minimum and the depth of the outer well. The experimental results provide a test for the *ab initio* calculations in the region of the well and confirm the accuracy of the theoretical long-range calculations. However, at smaller distances ($R \leq 15a_0$), very few experimental data are presently available to precise the exact position and the shape of the hump. The *ab initio* calculations predict a barrier $5.3\ cm^{-1}$ below the dissociation limit. On the contrary, the observation of a giant structure attributed to tunneling effect through the barrier seems to indicate that the maximum of the hump is located closer to or above the dissociation limit.

Due to the importance of the long-range behavior of the potential for the determination of the scattering length and atomic lifetimes, and of the barrier for the production of translationally cold molecules, further work should address these issues.

Informations are still lacking concerning the inner well and the barrier between the two wells. More data from photoassociation experiments would hardly offer possibilities for further investigations of the $0_g^-$ state in this region because near the dissociation limit, the experimental resolution is limited by the hyperfine structure leading to a quasi-continuum of states. It will be too difficult to get an experimental answer about the evolution of the inner classical turning point by this way. Moreover, the present fitting procedure is no longer appropriate as the energy of the highest levels in molecular potentials should not be described through the usual JWKB quantization formula [57,58]. Direct spectroscopic determination of the inner well is therefore necessary and could be obtained for instance by Fourier transform spectroscopy.

The authors are grateful to L. Cabaret for precious help with the Ti:sapphire laser operation, and to Prof. W. Meyer for kindly providing cesium dimer potential curves. Discussions with M. Allegrini, A. Crubellier, J. Pinard, and J. Vergès are gratefully acknowledged. A. Fioretti is the recipient of an European TMR grant, contract no. ERBFMBICT961218.

## References

1. H. Margenau, Rev. Mod. Phys. **11**, 1 (1939).
2. H.R. Thorsheim, J. Weiner, P.S. Julienne, Phys. Rev. Lett. **58**, 2420 (1987).
3. M.H. Anderson, J.R. Ensher, M.R. Matthews, C.E. Wieman, E.A. Cornell, Science **269**, 198 (1995).
4. K.B. Davis, M.-O. Mewes, M.R. Andrews, N.J. van Druten, D.S. Durfee, D.M. Kurn, W. Ketterle, Phys. Rev. Lett. **75**, 3969 (1995).
5. C.C. Bradley, C.A. Sackett, J.J. Tollett, R.G. Hulet, Phys. Rev. Lett. **75**, 1687 (1995).
6. P.D. Lett, P.S. Julienne, W.D. Philips, Annu. Rev. Phys. Chem. **46**, 423 (1995).
7. J. Weiner, Adv. At. Mol. Opt. Phys. **35**, 45 (1995); J. Weiner, V.S. Bagnato, S. Zilio, P.S. Julienne, Rev. Mod. Phys. (in press, 1999).
8. A. Fioretti, D. Comparat, A. Crubellier, O. Dulieu, F. Masnou-Seeuws, P. Pillet, Phys. Rev. Lett. **80**, 4402 (1998).
9. K.M. Jones, S. Maleki, S. Bize, P.D. Lett, C.J. Williams, H. Richling, H. Knöckel, E. Tiemann, H. Wang, P.L. Gould, W.C. Stwalley, Phys. Rev. A **54**, R1006 (1996).
10. W.I. McAlexander, E.R.I. Abraham, R.G. Hulet, Phys. Rev. A **54**, R5 (1996).
11. K.M. Jones, P.S. Julienne, P.D. Lett, W.D. Phillips, E. Tiesinga, C.J. Williams, Europhys. Lett. **35**, 85 (1996).
12. H. Wang, J. Li, X.T. Wang, C.J. Williams, P.L. Gould, W.C. Stwalley, Phys. Rev. A **55**, R1569 (1997).
13. W.C. Stwalley, Y.H. Uang, G. Pichler, Phys. Rev. Lett. **41**, 1164 (1978).

14. I. Mourachko, D. Comparat, F. de Tomasi, A. Fioretti, P. Nosbaum, V.M. Akulin, P. Pillet, Phys. Rev. Lett. **80**, 253 (1998).
15. C. Monroe, W. Swann, H. Robinson, C. Wieman, Phys. Rev. Lett. **65**, 1571 (1990).
16. S. Grego, M. Colla, A. Fioretti, J.H. Müller, P. Verkerk, E. Arimondo, Opt. Commun. **132**, 519 (1996).
17. S. Gerstenkorn, J. Vergès, J. Chevillard, *Atlas du spectre d'absorption de la molecule d'iode* (Laboratoire Aimé Cotton, Orsay, France, 1982).
18. G. Avila, P. Gain, E. de Clerq, P. Cerez, Metrologia **22**, 111 (1986).
19. V. Sanchez-Villicana, S.D. Gensemer, P.L. Gould, Phys. Rev. A **54**, R3730 (1996).
20. R. Côté, A. Dalgarno, Y. Sun, R.G. Hulet, Phys. Rev. Lett. **74**, 3581 (1995).
21. P.S. Julienne, J. Res. Natl. Inst. Stand. Technol. **101**, 487 (1996).
22. P. Pillet, A. Crubellier, A. Bleton, O. Dulieu, P. Nosbaum, I. Mourachko, F. Masnou-Seeuws, J. Phys. B **30**, 2801 (1997).
23. M. Arndt, M. Ben Dahan, D. Guéry-Odelin, M.W. Reynolds, J. Dalibard, Phys. Rev. Lett. **79**, 625 (1997).
24. B.J. Verhaar, K. Gibble, S. Chu, Phys. Rev. A **48**, R3429 (1993).
25. M.E. Wagshul, K. Helmerson, P.D. Lett, S.L. Rolston, W.D. Philips, R. Heather, P.S. Julienne, Phys. Rev. Lett. **70**, 2074 (1993).
26. H. Wang, P.L. Gould, W.C. Stwalley, J. Chem. Phys. **106**, 7899 (1997).
27. A. Fioretti, D. Comparat, C. Drag, T.F. Gallagher, P. Pillet, Phys. Rev. Lett. (in press, 1999).
28. X. Wang, H. Wang, P.L. Gould, W.C. Stwalley, Phys. Rev. A **57**, 4600 (1998).
29. M. Marinescu, A. Dalgarno, Phys. Rev. A **52**, 311 (1995).
30. M. Marinescu, A. Dalgarno, Z. Phys. D **36**, 239 (1996).
31. J.W. Tromp, R.J. Le Roy, J. Mol. Spectrosc. **109**, 352 (1985).
32. E. Tiesinga, C.J. Williams, P.S. Julienne, K.M. Jones, P.D. Lett, W.D. Phillips, J. Res. Natl. Inst. Stand. Technol. **101**, 505 (1996).
33. J.L. Dunham, Phys. Rev. **41**, 721 (1932).
34. C.W. Mathews, K.N. Rao, *Molecular Spectroscopy: Modern Research* (Academic Press, Inc. US, 1972).
35. R.J. Le Roy, R.B. Bernstein, J. Chem. Phys. **52**, 3869 (1970).
36. W.C. Stwalley, Chem. Phys. Lett. **6**, 241 (1970).
37. W.C. Stwalley, J. Chem. Phys. **58**, 3867 (1973).
38. B. Ji, C.C. Tsai, Li Li, T.J. Whang, A.M. Lyyra, H. Wang, J.T. Bahns, W.C. Stwalley, R.J. Le Roy, J. Chem. Phys. **103**, 7240 (1995).
39. R.J. Le Roy, R.B. Bernstein, Chem. Phys. Lett. **5**, 42 (1970).
40. F. Martin, M. Aubert-Frécon, R. Bacis, P. Crozet, C. Linton, S. Magnier, A.J. Ross, I. Russier, Phys. Rev. A **55**, 3458 (1997).
41. C. Amiot, Chem. Phys. Lett. **241**, 133 (1995).
42. A.R. Hashemi-Attar, C.L. Beckel, W.N. Keepin, S.A. Sonnleitner, J. Chem. Phys. **70**, 3881 (1979).
43. C.L. Beckel, R.B. Kwong, A.R. Hashemi-Attar, R.J. Le Roy, J. Chem. Phys. **81**, 66 (1984).
44. R.J. Le Roy, W.H. Lam, Chem. Phys. Lett. **71**, 544 (1980).
45. J.W. Tromp, R.J. Le Roy, Can. J. Phys. **60**, 26 (1982).
46. Computer codes which perform the NDE fits were kindly supplied to C.A. by Professor Le Roy.
47. R.J. Rafac, C.E. Tanner, A.E. Livingston, K.W. Kukla, H.G. Berry, C.A. Kurtz, Phys. Rev. A **50**, R1976 (1994).
48. R.J. Le Roy, University of Waterloo Report, Chemical Physics Research Report, p. 425 (1993).
49. R.J. Le Roy, University of Waterloo Report, Chemical Physics Research Report, p. 555 (1995).
50. E.I. Dashevskaya, A.I. Voronin, E.E. Nikitin, Can. J. Phys **47**, 1237 (1969).
51. M. Movre, G. Pichler, J. Phys. B: At. Mol. Opt. Phys. **10**, 2631 (1977).
52. B. Bussery, M. Aubert-Frécon, J. Chem. Phys. **82**, 3224 (1985).
53. H. Wang, P.L. Gould, W.C. Stwalley, Z. Phys. D **36**, 317 (1996).
54. M. Foucrault, Ph. Millié, J.P. Daudey, J. Chem. Phys. **96**, 1257 (1992).
55. N. Spiess, Ph.D. thesis, Fachbereich Chemie, Universität Kaiserslautern, 1989.
56. W. Meyer (private communication, 1989).
57. C. Boisseau, E. Audouard, J. Vigué, Europhys. Lett. **41**, 349 (1998).
58. J. Trost, C. Elshka, H. Friedrich, J. Phys. B: At. Mol. Opt. Phys. **31**, 361 (1998).